Philosophical Magazine,
Vol. 86, No. 36, 21 December 2006, 5805–5823

Taylor & Francis
Taylor & Francis Group

Comparison of off-axis and in-line electron holography as quantitative dopant-profiling techniques

A. C. TWITCHETT*, R. E. DUNIN-BORKOWSKI and P. A. MIDGLEY

Department of Materials Science and Metallurgy, University of Cambridge, Pembroke Street, Cambridge, CB2 3QZ, UK

(*Received 22 December 2005; in final form 10 March 2006*)

Many different dopant-profiling techniques are available for semiconductor device characterization. However, with length scales shrinking rapidly, only transmission electron microscopy (TEM) techniques promise to fulfil the spatial resolution required for the characterization of future device generations. Here, we use three advanced TEM techniques, off-axis electron holography, Fresnel imaging (in-line electron holography) and Foucault imaging, to examine a focused ion beam-prepared silicon *p–n* junction device. Experiments are carried out on electrically unbiased samples and with an electrical bias applied *in situ* in the TEM. Simulations are matched to experimental data to allow quantitative conclusions to be drawn about the underlying electrostatic potential distributions. The off-axis electron holography and Fresnel results are compared to assess whether the techniques are consistent, and whether they can be used to provide complementary information about dopant potentials in semiconductor devices.

1. Introduction

For over 30 years, transmission electron microscopy (TEM) techniques have been used to characterise electrostatic potential distributions arising from the presence of dopant atoms in semiconductors [1–3]. Variations in the electrostatic potential generate changes in phase shift of the electron wave that cannot be detected in standard in-focus electron micrographs. Phase contrast techniques, such as electron holography, must, therefore, be used for dopant characterization. Of the different electron holography techniques available [4], the most commonly used forms are off-axis electron holography and in-line electron holography (Fresnel imaging). These techniques make use of interference effects to detect a phase change between coherent electrons that have passed through or outside a sample. The phase change of an electron wave passing through an electrostatic potential distribution can be described using the equation:

$$\phi(x, y) = C_E \int V(x, y, z)\mathrm{d}z \qquad (1)$$

*Corresponding author. Email: act27@cam.ac.uk

Philosophical Magazine
ISSN 1478–6435 print/ISSN 1478–6443 online © 2006 Taylor & Francis
http://www.tandf.co.uk/journals
DOI: 10.1080/14786430600815385

where V is the electrostatic potential, z is a direction parallel, and x and y are directions perpendicular to the incident electron beam, and C_E is a specimen-independent constant that takes a value of 7.3×10^6 rad/V/m at a microscope accelerating voltage of 200 kV.

Some of the first experiments were carried out by Titchmarsh *et al.* [1], who used Foucault imaging to examine the change in electrostatic potential across a *p–n* junction. Merli *et al.* [2] subsequently demonstrated the use of the out-of-focus technique (in-line electron holography) to examine a reverse-biased semiconductor *p–n* junction, but quantitative information could not be revealed about the junction properties. Off-axis electron holography was first applied to semiconductor devices by Merli *et al.* [5], who showed that the electrostatic potential associated with a reverse-biased *p–n* junction could be observed directly in the form of distortions of the interference fringes. In the latter study, the holograms covered a small field of view and contained few interference fringes, and quantitative information about the dopant distribution could not be obtained. This work led to modelling of the internal and external electrostatic potentials arising from *p–n* junctions, but little comparison with experimental results was carried out. Frabboni *et al.* [6] examined reverse-biased *p–n* junctions using off-axis electron holography and showed that electron holography could be used to obtain maps of the external electrostatic potential variation close to the position of a reverse-biased *p–n* junction. McCartney *et al.* [3] also examined *p–n* junctions using off-axis electron holography, but the quality of the data was limited by phase noise and sample geometry and defects.

More recently, Rau *et al.* [7] used off-axis electron holography to determine two-dimensional dopant profiles in both *p*- and *n*-MOS transistor structures. This work demonstrated the potential of electron holography as a technique for the characterization of semiconductor device structures. This paper introduced the concept of electrically 'dead' layers of thickness ~50 nm at the sample surfaces, whose nature and extent are now known to depend on the TEM sample preparation technique used (amongst other factors). McCartney *et al.* [8] examined a silicon *p–n* junction prepared using tripod (wedge) polishing and limited Ar ion-beam milling, and reported the absence of electrically 'dead' layers at the sample surfaces.

Electron holography is used to measure the potential projected in the beam direction, including the external electrostatic potential above and below the sample. This projection makes it difficult to assess the impact of the variations in potential close to the specimen surfaces on results obtained using electron holography. The examination of focused ion beam (FIB) milled semiconductors using off-axis electron holography is of great interest to the semiconductor industry as this technique allows TEM specimens to be prepared rapidly from site-specific regions of device structures. Off-axis electron holography has previously been used to examine the two-dimensional phase distribution from a FIB-milled Si *p–n* junction [9].

Here, we compare the application of Fresnel (out-of-focus) imaging, Foucault imaging and off-axis electron holography as methods for the examination of the electrostatic potential arising from a silicon *p–n* junction. The consistency of the experimental results obtained using these techniques is assessed. FIB-prepared specimens are examined both unbiased and under an applied bias *in situ* in the TEM. The experimental results are fitted to simulations to obtain best-fitting parameters

for the dopant-dependent electrostatic potential distribution in the specimen. Some of the off-axis electron holography results have been presented in preliminary form elsewhere [10, 11].

2. TEM-based dopant-profiling techniques

Figure 1a shows a schematic diagram illustrating the formation of an off-axis electron hologram. The application of a positive voltage to an electron biprism, which is located close to a conjugate imaging plane of the microscope, allows an electron wave that has passed through the region of interest on the sample to be overlapped with another part of the same electron wave that has passed only through vacuum. An overlap width of 1–2 μm and a holographic interference fringe spacing of below 10 nm can be achieved by using a 'Lorentz' mini-lens as the main focusing lens, in place of the conventional TEM objective lens. The intensity distribution in

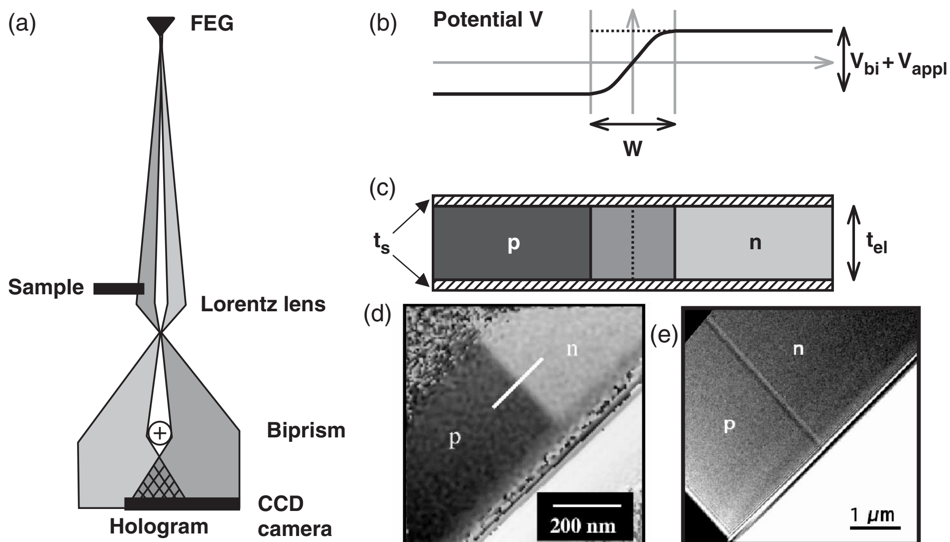

Figure 1. (a) Schematic diagram showing the experimental setup required for the formation of off-axis electron holograms. (b) Schematic diagram showing the electrostatic potential profile across a symmetrical semiconductor *p–n* junction. V_{bi} is the built-in voltage across the junction and W is the width of the depletion region over which the potential changes. The sign convention for the potential is consistent with the mean inner potential of the sample being positive relative to vacuum. (c) Schematic diagram showing the cross-sectional geometry of a TEM sample that contains a *p–n* junction. t_{el} is the 'electrically active' sample thickness. The electron beam direction is towards the bottom of the page. The shaded areas at the top and bottom surfaces of the sample of total thickness t_s represent electrically passivated or depleted layers, whose physical and electrical nature is affected by TEM sample preparation. (d) Phase image reconstructed from an off-axis electron hologram acquired from a 550-nm thick FIB-prepared Si *p–n* junction specimen. (e) An overfocus bright-field energy-filtered zero-loss image (Fresnel image) of a 410-nm thick specimen of the same Si *p–n* junction.

the interference pattern (the 'hologram') contains information about both the phase and the amplitude of the electron wave that has been affected by the electrostatic potential distribution in the specimen. This information can be extracted from the hologram by using a reconstruction process that is described in detail elsewhere [12].

Figures 1b and c show schematic diagrams of the electrostatic potential distribution that is expected to be present at a *p–n* junction in a thin TEM specimen [13]. Figure 1d shows an experimental phase image of an FIB-milled membrane reconstructed from an off-axis electron hologram of a silicon *p–n* junction. The step in phase across the junction $\Delta\phi$ can in principle be related to the built-in voltage V_{bi} by using the equation:

$$\Delta\phi = C_{\mathrm{E}}(V_{\mathrm{bi}} + V_{\mathrm{appl}})t_{\mathrm{el}} \tag{2}$$

where V_{appl} is the electrical bias applied to the junction and t_{el} is the 'electrically active' specimen thickness, given by $(t_{\mathrm{total}} - t_{\mathrm{s}})$, where t_{total} is the total specimen thickness and t_{s} is the total thickness of the layers on the specimen surfaces that do not contribute to the measured phase change (figure 1c). The proposed electrostatic potential variation and the separation of crystalline and electrically active membrane thicknesses are consistent with previous reports [9–11]. Equation (2) assumes that the external electric field is negligible, that the reference wave passes through unperturbed vacuum and that the electrical properties of the specimen are constant in the beam direction within specimen thickness t_{el}. These assumptions are discussed further below.

In-line electron holography, or Fresnel imaging [14], can also be used to obtain information about the phase change of the electron wave that has passed through a thin specimen. By recording a defocused bright-field image (see figure 1e), an interference pattern is formed from the scattered and unscattered electron waves that have passed through the sample. Fresnel interference fringes form at positions of rapid variations in electrostatic potential in the specimen and can, therefore, be observed at *p–n* junctions. The positions of the fringes and their intensities can be examined as a function of defocus to obtain information about the underlying potential variation. Here, we match experimental defocus series with simulated Fresnel fringe profiles [15].

Both Fresnel imaging and off-axis electron holography are sensitive to the electrostatic potential distribution in a semiconductor sample. However, Fresnel imaging provides higher spatial resolution information about the junction profile, due to both the amplification and lateral spreading of the contrast with defocus and the improved signal-to-noise ratio that results from the acquisition of a defocus series of images.

As in-line and off-axis electron holography are sensitive to the same variation in potential, it is important to confirm that results obtained from the same sample using the two techniques are consistent. It is also important to establish whether the two techniques can be used to provide complementary information, as off-axis electron holography is sensitive to a wide range of spatial frequencies in the electrostatic potential, whereas Fresnel imaging is comparatively insensitive to low spatial frequencies but very sensitive to rapid changes in potential.

The change in electrostatic potential arising from a *p–n* junction can also be observed in a diffraction pattern of the area containing the junction, in the form of streaking of the diffraction spot. By ensuring that the objective aperture is accurately positioned in the back focal plane, either the spot or the streak can be selected to allow the formation of a bright- or a dark-field image (respectively) of the region of varying electrostatic potential. Such images cannot be interpreted directly to obtain the underlying electrostatic potential variation, but they can be compared with simulations of the expected contrast to deduce further information about the junction potential. As Foucault imaging is extremely sensitive to the position of the aperture that is used to mask either the spot or the streak, it is most suited to qualitative examination of the electrostatic potential.

3. Experimental details

A {100} silicon wafer containing a *p–n* junction 2.5 μm below the wafer surface was prepared for TEM examination using an FEI 200 FIB workstation. The nominal dopant concentrations were $5 \times 10^{18}\,\mathrm{cm}^{-3}$ in both the *p*-type (B-doped) and the *n*-type (Sb-doped) layers. Four different membrane thicknesses were prepared in standard trench (H-bar) geometry in the FIB workstation, while a new specimen geometry (figure 2a) was developed for biasing experiments [9]. For biasing, the specimen was prepared by FIB milling a cleaved 1–2 mm square of wafer parallel to the growth direction of the wafer to leave a parallel-sided membrane at a corner of the cleaved wedge. Extra cuts (figure 2b) were milled to provide an area of vacuum close to the region of interest for off-axis electron holography. Figure 2c shows a schematic diagram of the biasing holder, which was designed and constructed to allow the application of two electrical spring contacts to the sample *in situ* in the TEM.

Off-axis electron holograms were acquired at 200 kV using a Philips CM300 field emission gun (FEG) TEM operated in Lorentz mode. Samples were tilted to align the junction parallel to the electron beam but at a condition that minimized diffraction contrast from the area of interest. As the membranes were of uniform thickness and unstrained, the diffraction condition was uniform across the field of view. Holograms with ∼1 μm interference width and a fringe spacing of 5–10 nm were acquired using a 2048 pixel charge coupled device (CCD) camera and a positive biprism voltage of 80–100 V. Electrical biasing experiments were performed by applying reverse bias voltages of 0, 1, 2 and 3 V to the specimen. The holograms were reconstructed using programs written in the Semper image processing language [16]. Line profiles across the junction were extracted from each phase image and from each Fresnel image (e.g. along the white line shown in figure 1d).

From equation (2), it is apparent that an accurate knowledge of the specimen thickness is required to interpret experimental electron holography results quantitatively. Accordingly, the crystalline thickness of each specimen was determined using energy-filtered convergent beam electron diffraction (CBED), with the crystal tilted to a two-beam condition with $\boldsymbol{g} = 400$, using a 10-eV energy-selecting slit width. The crystalline specimen thicknesses were determined to be 220,

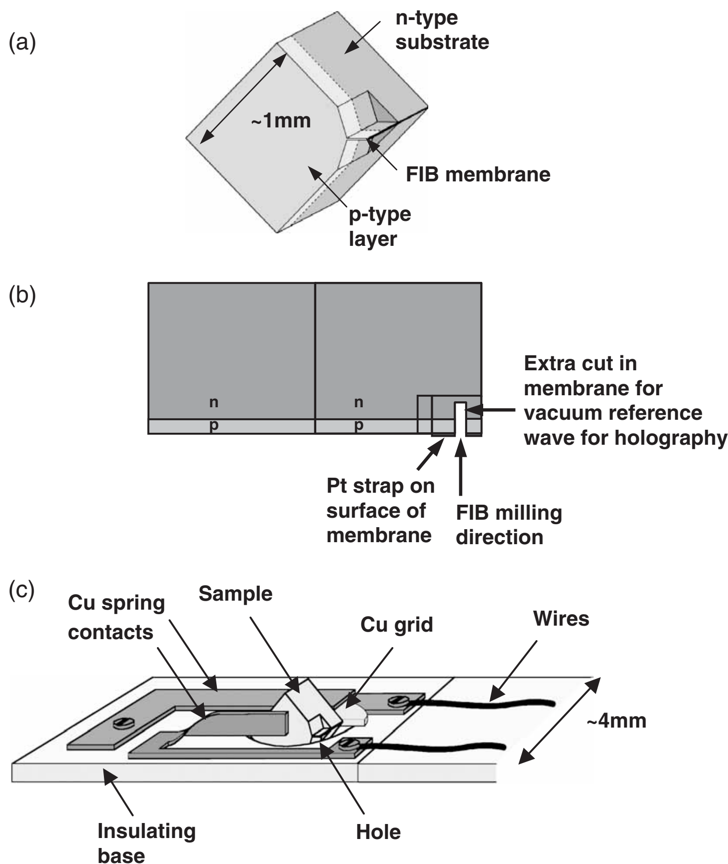

Figure 2. (a) Schematic diagram showing the sample geometry for electrical biasing experiments. The sample is prepared by cleaving a 1–2-mm square of wafer, one corner of which is subsequently focused ion beam milled parallel to the original wafer growth direction. (b) Schematic diagram (not to scale) showing the Pt strap and the extra cut, made by focused ion beam milling, for the vacuum reference wave required for off-axis electron holography. (c) Schematic diagram of the electrical biasing holder with the sample in place. The sample is glued to the edge of a Cu grid using conducting epoxy and then clamped between two spring contacts on an insulating base.

270, 410 and 550 nm for the unbiased samples, and 390 nm for the biased sample. Additional measurements of the total (amorphous and crystalline) specimen thickness were obtained from the reconstructed amplitude images, in units of inelastic mean free path.

Bright-field zero-loss-energy-filtered Fresnel images of each sample were acquired using the same microscope, with defocus values of between -3.5 and $+3.5$ mm. The microscope was operated in Lorentz mode at 200 kV at a nominal magnification of 380×, corresponding to a field of view in each image of between 3 and 6 μm. An energy-selecting slit width of 10 eV was used, with an acquisition time of 8 s. Fresnel defocus series were acquired both from the unbiased specimens and using reverse bias voltages of 1, 2 and 3 V.

Bright- and dark-field Foucault images of the *p–n* junction were acquired from the Si 400 diffraction spot, using an objective aperture to select either the central section of the diffraction spot to form a bright-field Foucault image, or the streak arising from the change in electrostatic potential across the junction to form a dark-field Foucault image.

4. Experimental results

Bright- and dark-field Foucault images acquired from the 550-nm thick unbiased membrane are shown in figure 3. The position of the *p–n* junction is revealed clearly in these images as a bright or dark line. However, as mentioned above, this technique cannot be used to provide quantification of the underlying junction parameters, such as charge density and depletion width, owing to its sensitivity to the aperture position in the back focal plane and the strong defocus dependence of both the intensity and the bright and dark contrast. Therefore, this technique will not be considered further in the present study.

Figure 4 shows line profiles extracted from phase images obtained from off-axis electron holograms of the Si *p–n* junction, for (a) the unbiased membranes and (b) the biased membrane for different values of reverse bias voltage. Values of the step in phase across the junction and the depletion width can be obtained from these plots, as discussed below. However, if the electrostatic potential associated with the dopant distribution varies in the specimen in the electron beam direction, or if the junction is not perfectly abrupt, then these two parameters alone are not sufficient to describe the junction. Poisson's equation allows a measure of the electric field and charge density to be calculated from a measured projected electrostatic potential profile across a *p–n* junction by differentiation. However, experimental phase profiles

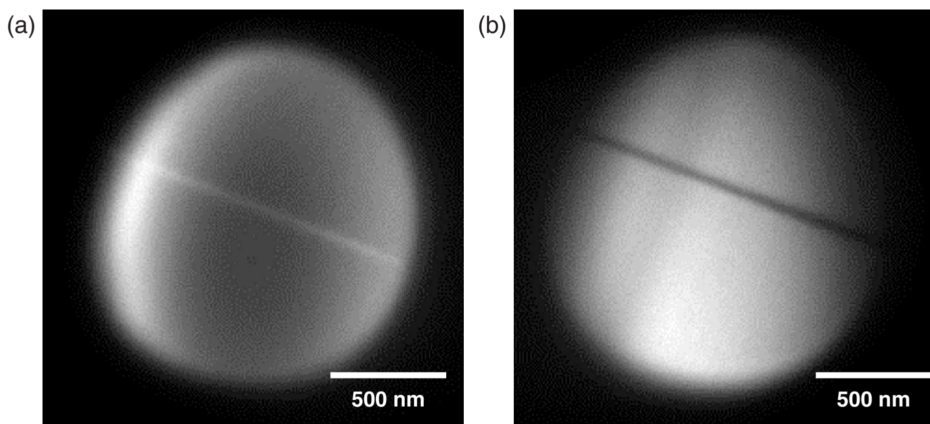

Figure 3. Foucault images of the 550-nm thick Si *p–n* junction specimen obtained by using the objective aperture to select (a) the streak from the *p–n* junction, with the unscattered beam masked out, and (b) the unscattered beam, with the streak from the *p–n* junction masked out.

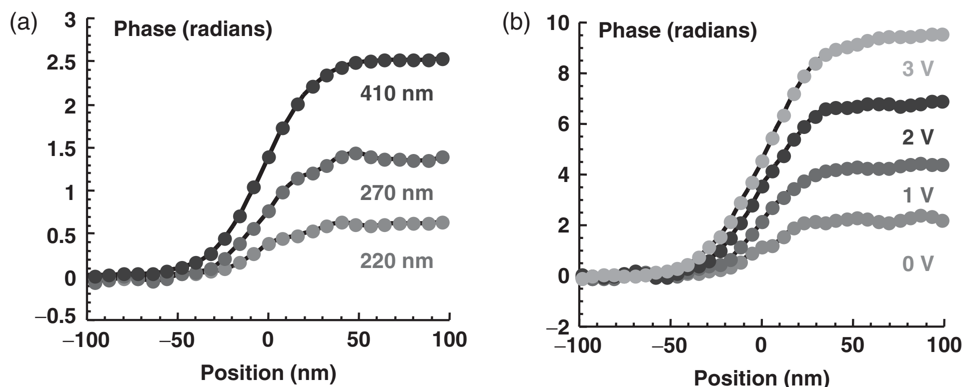

Figure 4. Line profiles showing the measured phase shift across the Si *p–n* junction, plotted as a function of (a) sample thickness (measured using CBED) for three different unbiased samples, and (b) reverse bias voltage for a single sample whose crystalline thickness was measured to be 390 nm. The images have been averaged over a distance of approximately 25 nm along the junction to form these profiles.

obtained using off-axis electron holography are often too noisy for this approach to provide useful information directly. Instead, the experimental phase profiles can be fitted to simulations (described below), from which the electric field and charge density profiles are then obtained. Different models for the electrostatic potential variation across the junction and through the thickness of the TEM membrane can be assessed in this way.

Figure 1e shows a bright-field energy-filtered image of the Si *p–n* junction in a 410-nm thick specimen, acquired at 3.5 mm overfocus in Lorentz mode. A defocus series of Fresnel images of an unbiased specimen containing the *p–n* junction is shown in figure 5, alongside projected line profiles of the recorded intensity. The line profiles have been normalized by dividing them by the background intensity in each image. The spreading of the interference fringes from the position of the junction with increasing defocus is apparent in figure 5. The intensity profiles cannot be interpreted directly to provide information about the underlying electrostatic potential variation. Instead, simulations of the intensity variation with defocus were fitted to the experimental line profiles. By using the same models to fit simulations to the off-axis and in-line electron holography results, a direct comparison of the potential variation across the junction measured using the two techniques could be obtained.

5. Best-fitting simulations

Simulations of Fresnel defocus images and phase images were performed by using a single phase grating approximation to the multislice algorithm. Three different models were used to describe the electrostatic potential distribution, both across the *p–n* junction and through the thickness of the TEM membrane.

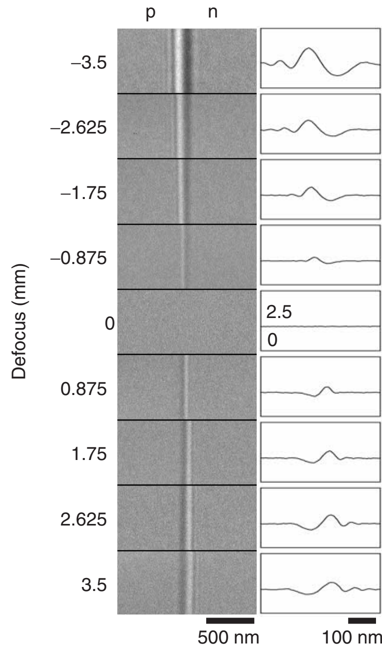

Figure 5. Montage of regions extracted from Fresnel images of the unbiased Si *p–n* junction, from a 550-nm thick specimen, displayed as a function of defocus, with corresponding line profiles obtained by projecting the contrast parallel to the junction.

Best-fitting profiles to the experimental results were obtained by choosing parameters describing the specimen and the imaging parameters using a Simplex algorithm [17] and minimizing the squared difference between the simulations and the experimental profiles. Figure 6 shows an outline of the fitting routine for in-line electron holography. The variable parameters include the depletion width, the built-in voltage across the junction, the electrically active specimen thickness and the abruptness of the junction profile. Some of the variable parameters, such as the built-in voltage and the electrically active specimen thickness, clearly have a similar effect on the potential profile. It is, therefore, necessary to fix one of these parameters to an independently calibrated value for the purpose of the simulations. Electric field and charge density profiles were calculated using Poisson's equation from the fitted projected electrostatic potential. Variations in absorption contrast across the region of interest were not considered, as neither the composition nor the diffracting condition of the sample varies significantly across the junction. The beam convergence and the lateral position of each profile within a Fresnel defocus series were also fitted. Beam convergence is known to affect the observed contrast in Fresnel profiles [15] and, therefore, it could either be fitted or left as a known, calibrated parameter for the simulations. However, for the experimental conditions used here, the beam convergence is extremely small; therefore the simulations were optimized with a fixed beam convergence of zero.

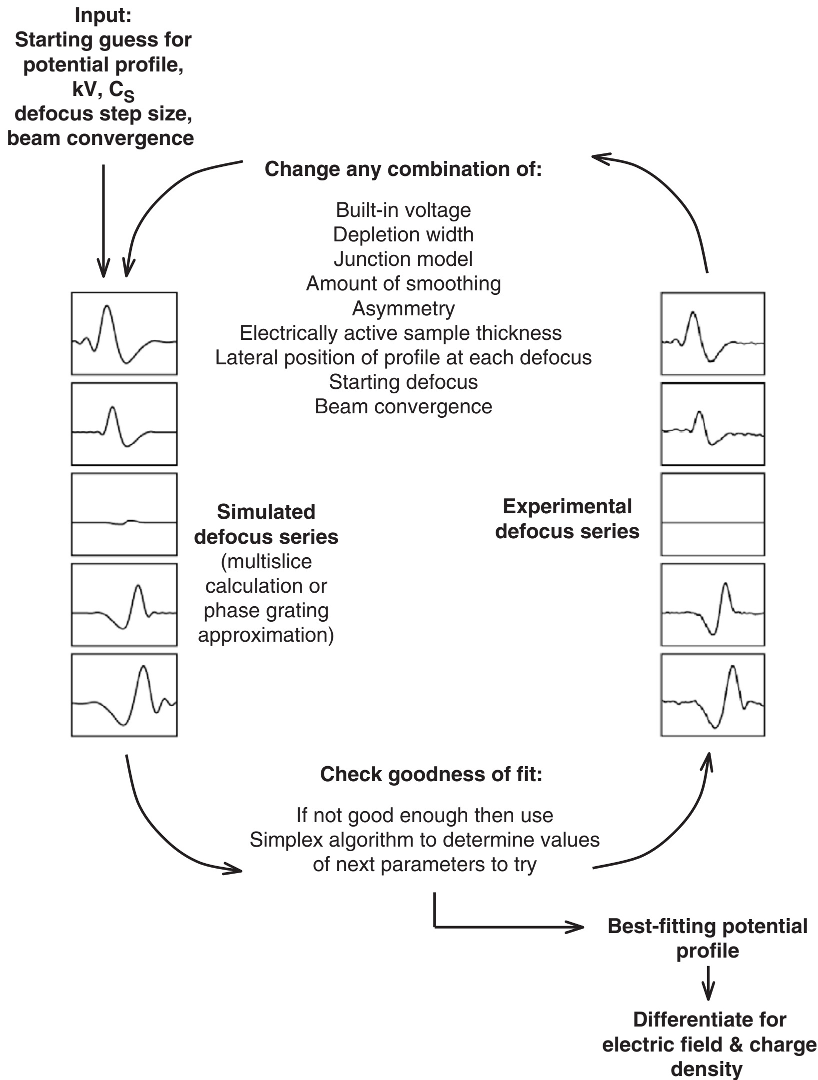

Figure 6. Outline of the fitting algorithm used to find a best-fitting potential profile to a Fresnel defocus series of profiles of the energy-filtered bright-field zero-loss intensity measured across a *p–n* junction. The parameters that describe the junction profile are selected at each iteration using a Simplex algorithm, and the fit to the experimental data is assessed using the mean of the squared differences between the experimental and simulated profiles. The best-fitting potential profile is differentiated to determine the electric field and the charge density across the *p–n* junction.

6. Discrepancies and similarities between off-axis electron holography and Fresnel imaging

Figure 7a shows experimental Fresnel fringe profiles obtained from four unbiased specimens. Figure 7b shows corresponding simulations generated from phase profiles

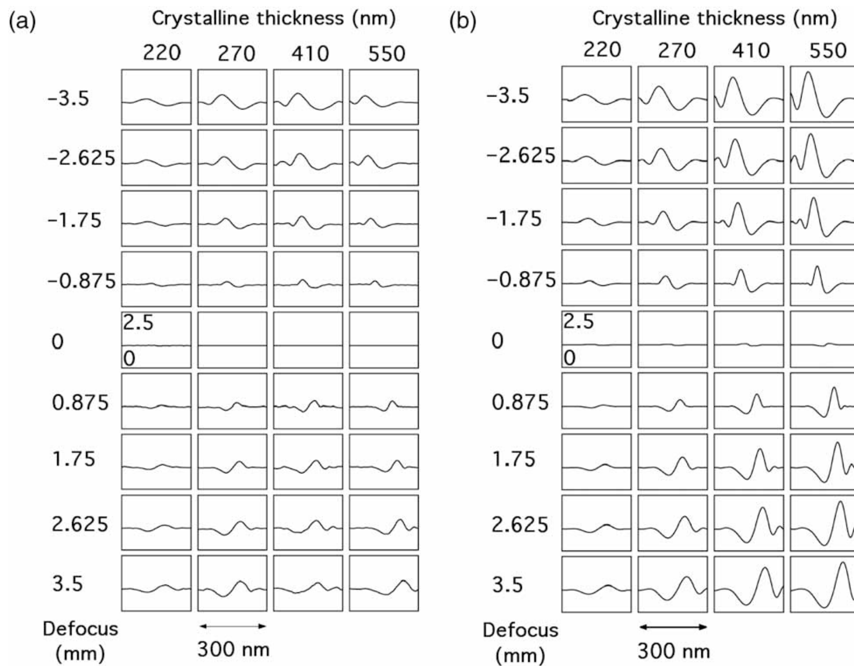

Figure 7. (a) Experimental Fresnel defocus series of intensity profiles measured across *p–n* junctions in four unbiased focused ion beam milled samples of different thickness. The mean intensity has been scaled to unity in each profile. (b) Simulated profiles determined from phase images measured from the same samples using off-axis electron holography, showing the discrepancy between the magnitude of the simulated contrast and that of the raw experimental Fresnel profiles. The discrepancy increases with sample thickness.

measured from off-axis electron holograms acquired from the same samples. Surprisingly, despite the fact that the Fresnel images were energy-filtered, the contrast of the experimental fringes is considerably lower and, therefore, appears to correspond to a much smaller electrically active thickness than would be required for consistency with the off-axis data recorded from the same samples. This point is illustrated in figure 8, which shows a plot of the fitted electrically active thickness from the raw experimental Fresnel contrast on the assumption of a built-in voltage across the junction of 0.9 V. Rather than a straight line with a slope of unit of unity, the graph rises more slowly than expected and then starts to drop.

To reconcile the discrepancy between the off-axis and in-line results, the presence of a uniform background in the Fresnel images arising from diffuse scattering was assumed. The contrast of the Fresnel defocus images was adjusted by using the same constant, n, for each defocus series, but varying n as required with sample thickness, according to the equation:

$$I_{\mathrm{new}} = \left(\frac{I_{\mathrm{old}} - n}{1 - n} \right) \tag{3}$$

where I_{old} and I_{new} are the intensities before and after removal of the background, respectively. Figure 9a shows the uniform background intensity that needed to be

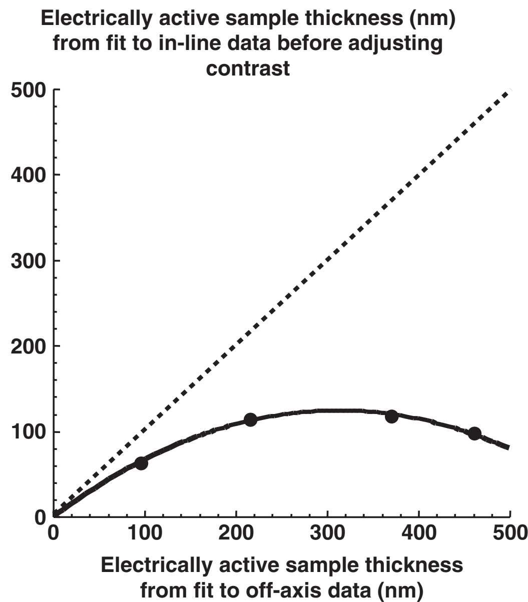

Figure 8. Graph showing the electrically active sample thickness that would be inferred from the raw (unscaled) experimental energy-filtered Fresnel contrast data, plotted as a function of the electrically active sample thickness inferred from off-axis electron holograms of the same samples. The dotted line has a gradient of 1, which would be the trend if the electrically active thickness obtained from off-axis and in-line holography results from the same specimen showed no discrepancy.

subtracted from each experimental Fresnel profile in order to match to the values of t_{el} and V_{bi} measured using off-axis electron holography. Figure 9b shows the rescaled experimental profiles, which now demonstrate excellent agreement with the simulated profiles (in figure 7b). The rescaled experimental profiles for the electrically biased membrane are shown in figure 10a, with corresponding simulated profiles in figure 10b. The fraction of the intensity that was removed is plotted as a function of the total sample thickness in figure 11a.

Figure 11a demonstrates that the fitted value of n increases approximately linearly with specimen thickness within the thickness range examined. The increase in n with sample thickness suggests that there is a contribution to the background intensity arising from the crystalline material present, as the amorphous layer thickness does not vary substantially between specimens. As n cannot exceed unity and appears to approach this value with increasing specimen thickness, an equation of the form $(1 - \exp(-t/\lambda))$ was fitted to the data, with a best-fitting value for λ of $\sim$600 nm.

The background intensity that is postulated here to explain the low contrast of the Fresnel images is reminiscent of that discussed for energy-filtered high-resolution lattice images [18], arising from diffuse scattering. Diffuse scattering may be associated with phonon excitations and defects in the crystal lattice, as well as with scattering in amorphous layers on the specimen surfaces [19]. Phonon scattering, in particular, which is associated with very small energy losses of $\sim 10^{-15}$ eV,

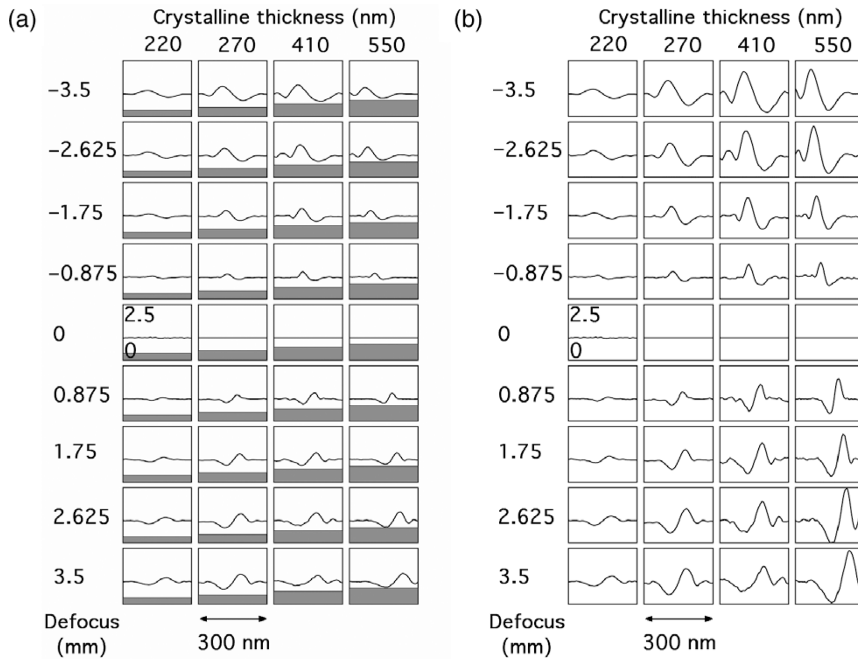

Figure 9. (a) The raw experimental Fresnel defocus series of figure 7a, showing the height of the uniform background that needs to be subtracted from each image for the experimental contrast to match that of the simulations. (b) The experimental profiles, now redisplayed after subtracting the uniform backgrounds shown in (a), and subsequently dividing each profile by its mean intensity.

is excluded from an image wave reconstructed from an off-axis electron hologram [20] but will be present in the Fresnel images acquired here. The phonon contribution to high-resolution images is found to either increase or decrease lattice fringe contrast, depending on the specimen thickness and defocus [21]. However, the specimens examined here are considerably thicker than those examined using high-resolution electron microscopy and they also have significantly thicker amorphous regions present on their surfaces arising from FIB milling. Little phonon scattering is expected in the amorphous layers themselves [21]. However, the proportion of phonon-scattered electrons is expected to increase with crystalline specimen thickness, as confirmed experimentally in figure 11b.

7. Quantification and comparison of experimental results obtained using off-axis and in-line holography

The depletion widths and charge densities that were inferred from the best-fitting potential profiles to the unbiased off-axis and scaled Fresnel data are plotted in figures 12a and b as a function of the electrically active specimen thickness. Figures 13a and b show the corresponding results for the biased membrane, plotted

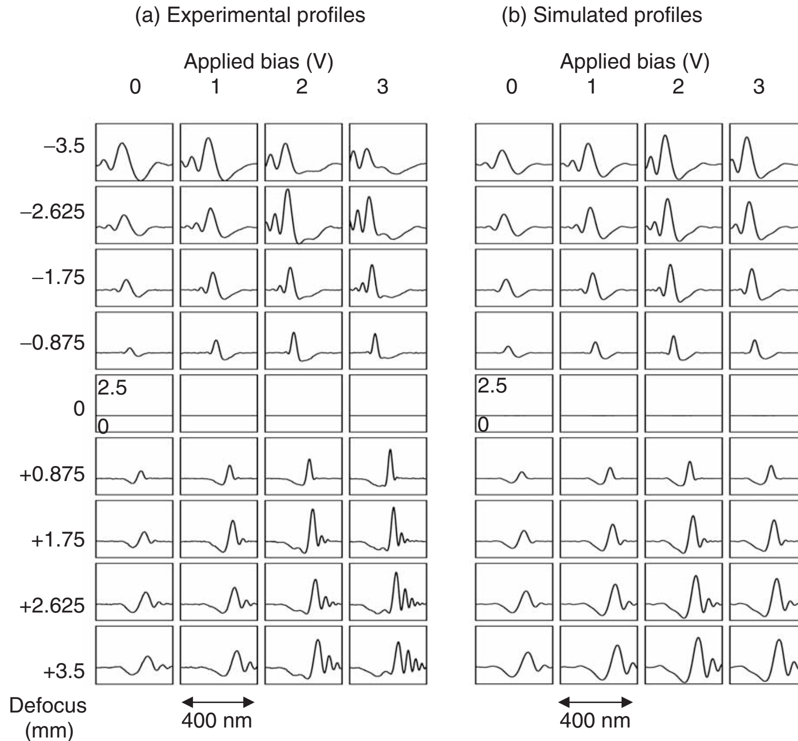

Figure 10. (a) Experimental Fresnel defocus series of intensity profiles measured across a Si *p–n* junction in a single reverse-biased focused ion beam milled sample whose crystalline thickness was measured to be 390 nm. The mean intensity has been scaled to unity in each profile after removing a uniform background intensity. (b) Simulated best-fitting profiles to the defocus series.

as a function of applied reverse bias. In each case, the results are consistent between the two techniques, although the scatter in the Fresnel data is much smaller than observed in the off-axis data, particularly for the unbiased results. This difference arises from the increased sensitivity to the high frequency potential variations across the junction and from the large number of data points fitted in each Fresnel series. As mentioned above, Fresnel imaging shows high sensitivity to rapidly varying electrostatic potential variations in the specimen, but poor sensitivity to low-frequency variations. Off-axis electron holograms detect all spatial frequencies with an equal sensitivity, but the spatial resolution across the junction is lower than can be obtained from Fresnel images. To optimize the spatial resolution in the reconstructed phase image, the spacing of the holographic interference fringes must be minimized, resulting in a reduction in the fringe contrast and, thus, reducing the attainable phase resolution [22]. Off-axis electron holography can, therefore, be used to determine the slowly varying potential to high accuracy by reconstructing holograms with relatively poor spatial resolution but good phase resolution, allowing the built-in voltage (or electrically active specimen thickness) to be determined. These holograms contain poor information about the detailed junction properties, such as the

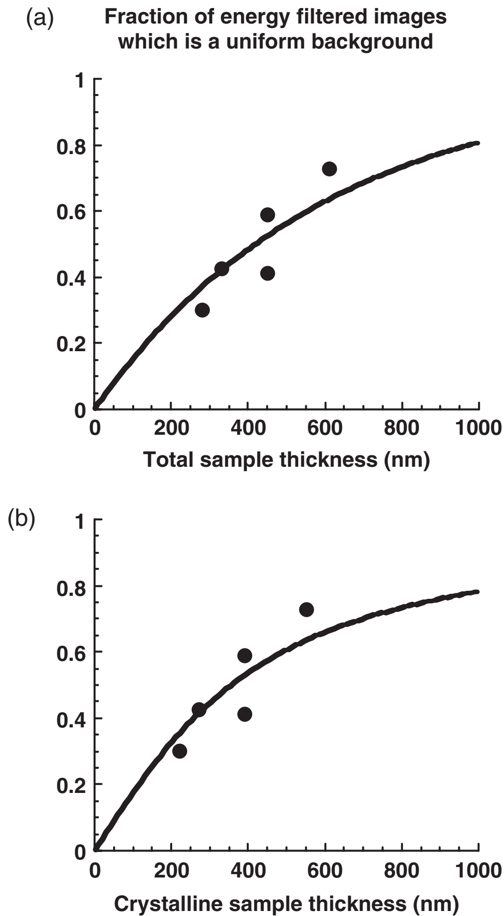

Figure 11. The fraction of the intensity in energy-filtered Fresnel defocus series of images of the Si *p–n* junction examined in this study that is inferred to comprise a uniform background for the fitted potential profile to be consistent with that measured from off-axis electron holograms of the same samples. The measurements are plotted as a function of (a) the total (crystalline and amorphous) sample thickness and (b) the crystalline sample thickness (determined using CBED).

depletion width and charge density, and, therefore, in-line holography can be used in parallel to provide this information.

In figure 13, the fitted charge density is considerably smaller than that expected from the nominal junction properties for the unbiased membranes, giving a value of $2 \pm 1 \times 10^{17}\,\mathrm{cm}^{-3}$, with a corresponding depletion width of $100 \pm 20\,\mathrm{nm}$, compared to expected values of $\sim 1 \times 10^{18}\,\mathrm{cm}^{-3}$ and 50 nm. Although some degeneracy may be expected in the semiconductor at such high dopant concentrations, resulting in a reduced electrically active dopant concentration, the fitted charge densities are still lower than expected. This decrease may result from sample preparation, as FIB milling is a destructive technique that is known to produce significant damage layers

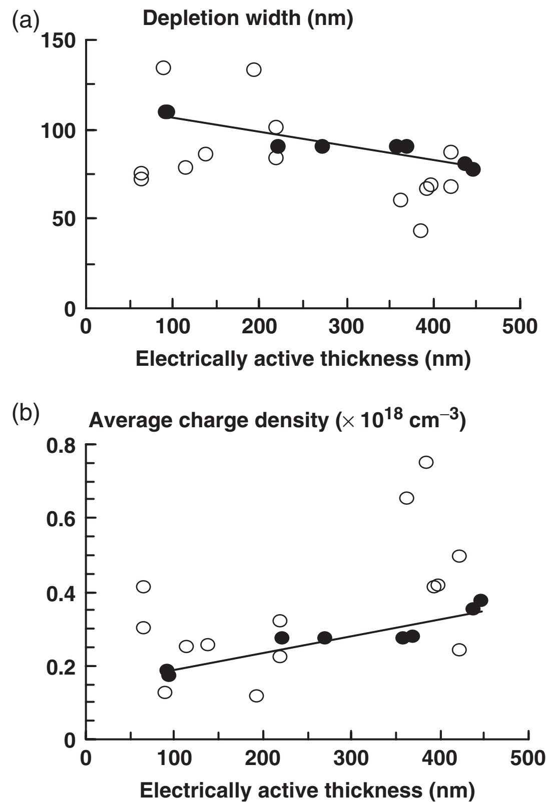

Figure 12. Comparison of (a) depletion widths and (b) charge densities in the depletion region of the Si *p–n* junction measured using both off-axis electron holography (open circles) and from Fresnel defocus series of images (black circles and lines) from a range of unbiased focused ion beam milled samples of different thickness (after removing a uniform background intensity).

on the membrane surfaces. These layers contain high concentrations of Ga atoms implanted by the ion beam [23], which may act to reduce the electrical activity of the semiconductor. Further investigation of the nature of this damage, including modelling of the physical and electrical properties of the FIB-prepared surfaces, is required.

The biased membrane data shows a much higher electrically active dopant charge density than the unbiased data, although the data point in the biased series at 0 V is consistent with the unbiased results. The fitted depletion widths are also much smaller than in the unbiased results, indicating that the application of an electrical bias to the semiconductor membrane has increased the concentration of active dopant atoms to a level that is more consistent with that expected from the nominal dopant concentration in this specimen. The electrically active dopant concentration is then increased to a level that is consistent with results obtained from samples prepared using cleaving [24]. Recent results have indicated that annealing of an F1B-prepared specimen may also increase the electrically active dopant concentration [25].

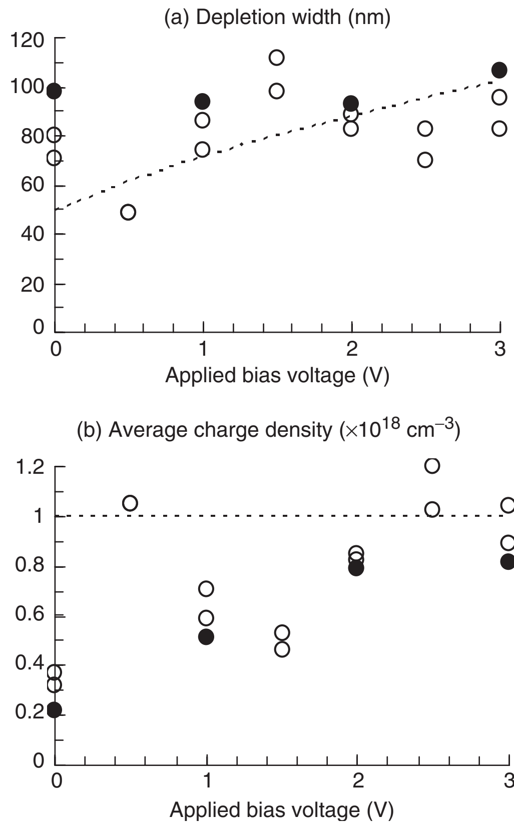

Figure 13. Comparison of (a) depletion widths and (b) charge densities from the 390-nm thick reverse biased Si *p–n* junction measured using both off-axis electron holography (open circles) and from Fresnel defocus series of images (black circles and lines) after removing a uniform background intensity. The dotted lines indicate the expected variation in depletion width and charge density with applied bias for an electrically active dopant concentration of $1 \times 10^{18}\,cm^{-3}$.

8. Conclusions

The electrostatic potential distribution across a silicon *p–n* junction has been examined using three different TEM-based techniques. Results obtained using in-line and off-axis electron holography demonstrated different sensitivities to the potential distribution. Off-axis holograms provided an accurate determination of the step in phase across the *p–n* junction in the FIB-prepared membranes, but provided poorer accuracy than Fresnel images in determining the depletion width or charge density profile across the junction. The energy-filtered Fresnel data acquired showed intensities that were inconsistent with the off-axis data until a uniform background, attributed to diffuse scattering, was removed. Fitting of the scaled results provided data that were consistent with the off-axis results.

These two holographic techniques can be used to extract quantitative information from experimental data. Off-axis electron holography is a more demanding technique experimentally, requiring specialist instrumentation. Two-dimensional maps of the electrostatic potential can be obtained using off-axis electron holography, whereas Fresnel imaging is best suited to the examination of a junction in one-dimension. The improved sensitivity of Fresnel imaging to the high-frequency potential information improves the accuracy of potential determination significantly. In conclusion, the application of these two techniques in parallel can be beneficial, but Fresnel imaging can only be used as a technique for quantitative dopant-profiling in semiconductor devices if the uniform background that must be subtracted from each image is determined independently using a technique such as off-axis electron holography. This conclusion has far wider implications for the quantitative interpretation of image intensities in all areas of transmission electron microscopy, even if energy-filtering is used.

Acknowledgements

The authors would like to thank Dr R. F. Broom for his assistance and advice, Philips Research Laboratories (Eindhoven) for providing the Si device and Newnham College, the Royal Society and the EPSRC for financial support.

References

[1] J.M. Titchmarsh, A.J. Lapworth and G.R. Booker, Phys. Status Solidi **34** K83 (1969).
[2] P.G. Merli, G.F. Missiroli and G. Pozzi, Phys. Status Solidi (a) **20** K87 (1973).
[3] M.R. McCartney, D.J. Smith, R. Hull, *et al.*, App. Phys. Lett. **65** 2603 (1994).
[4] J.M. Cowley, Ultramicroscopy **41** 335 (1992).
[5] P.G. Merli, G.F. Missiroli and G. Pozzi, J. Microsc. **21** 11 (1974).
[6] S. Frabboni, G. Matteucci and G. Pozzi, Ultramicroscopy **23** 29 (1987).
[7] W.D. Rau, P. Schwander, F.H. Baumann, *et al.*, Phys. Rev. Lett. **82** 2614 (1999).
[8] M.R. McCartney, M.A. Gribelyuk, J. Li, *et al.*, J. Appl. Phys. Lett. **80** 3213 (2002).
[9] A.C. Twitchett, R.E. Dunin-Borkowski and P.A. Midgley, Phys. Rev. Lett. **88** 8302 (2002).
[10] A.C. Twitchett, R.E. Dunin-Borkowski, R.F. Broom, *et al.*, J. Phys.: Condens. Matter **16** S181 (2004).
[11] A.C. Twitchett, R.E. Dunin-Borkowski, R.J. Hallifax, *et al.*, J. Microsc. **214** 287 (2004).
[12] E. Völkl, L.F. Allard and D.C. Joy (Editors), *An Introduction to Electron Holography* (Kluwer Academics/Plenum Press, New York, 1999).
[13] S.M. Sze, *Physics of Semiconductor Devices* (Wiley, New York, 1981).
[14] F. Ross and W.M. Stobbs, Phil. Mag. A **63** 1&37 (1991).
[15] R.E. Dunin-Borkowski, Ultramicroscopy **83** 193 (2000).
[16] W.O. Saxton, T.J. Pitt and M. Horner, Ultramicrosocopy **4** 343 (1979).
[17] W.H. Press, B.P. Flannery, S.A. Teukolsky, *et al.*, *Numerical Recipes in FORTRAN: The Art of Scientific Computing* (Cambridge University Press, Cambridge, 1992), pp. 402–406 and pp. 423–436.

[18] C.B. Boothroyd, J. Electron Microsc. **51** S279 (2002).
[19] C.B. Boothroyd and M. Yeadon, Ultramicroscopy **96** 361 (2003).
[20] D. Van Dyck, H. Lichte and J.C.H. Spence, Ultramicroscopy **81** 187 (2000).
[21] C.B. Boothroyd and R.E. Dunin-Borkowski, Ultramicroscopy **98** 115 (2004).
[22] H. Lichte, Ultramicroscopy **38** 13 (1991).
[23] J.P. McCaffrey, M.W. Phaneuf and L.D. Madsen, Ultramicroscopy **87** 97 (2001).
[24] A.C. Twitchett, Electron holography of semiconductor devices. PhD thesis, University of Cambridge (2002).
[25] D. Cooper, A.C. Twitchett, P.K. Somodi, *et al.*, App. Phys. Lett. **88** 063510 (2006).